Int. J. Electrochem. Sci., 17 **(2022)** Article Number: 220553, doi: 10.20964/2022.05.37

International Journal of
ELECTROCHEMICAL
SCIENCE
www.electrochemsci.org

MoO_2 Nanoparticles Decorated MoS_2 Nansheets Encapsulated on MXene as Advanced Anode for Ultrafast and Stable Lithium Ion Batteries

Jianhui He[1], *Chunrong Ma*[2], *Zhixin Xu*[2], *Daowu Zhou*[3]

[1] School of Materials Science and Engineering, Tongji University, Shanghai, 201804, China.
[2] School of Chemistry and Chemical Engineering, Shanghai Jiao Tong University, Shanghai, 200240, China.
[3] School of Materials Science and Engineering, Shanghai Jiao Tong University, Shanghai, 200240, China.
*E-mail: 15802196152@163.com

Received: 21 January 2022 / *Accepted:* 11 March 2022 / *Published:* 5 April 2022

Developing a facile and scalable strategy to implement the controlled synthesis of electrode materials is a huge challenge for realizing ultrafast and stable Li ion batteries. Herein, we designed and fabricate a 3D hierarchical architecture where carbon coated MoS_2/MoO_2 hybrid on MXene was used an advanced anode material for LIBs. The introduction of ultrafine MoO_2 nanoparticles helped to reduce the aggregation of MoS_2 nanosheets and decrease the Li^+ diffusion length. The good integration of 2D/2D composite into carbon can effectively accommodate the accompanying volume expansion and synergistically enhance the pseudocapacitive contribution to facilitate the reaction kinetics. The improved pseudocapacitive behavior guarantees a higher and more stable Li^+ ion storage performance. When evaluated as an anode in LIBs, the as-prepared electrode demonstrate superior rate capability of ~700 mAh g^{-1} at high current density of 10 A g^{-1} and outstanding cycling stability up to 800 cycles at a current density of 1A g^{-1}.

Keywords: Hierarchical structure, MoS_2, Anode, Electrochemical performance, Lithium ion batteries

1. INTRODUCTION

Lithium ion batteries (LIBs) as potential power sources have been widely used for portable electronic devices and electric vehicles. As a crucial component, anodes have a decisive impact on the electrochemical performance of LIBs.[1-3] Therefore, exploiting advanced anode materials with fast charge/discharge capability and cycling stability is pivotal in promoting next electric vehicles. However, practically the current commercial graphite cannot satisfy demand for the LIBs due to its low theoretical

capacity. Thus, various electrochemically active materials such as transition metal sulfides/oxides,[4-7] tin,[8, 9] titanium dioxide,[10, 11] and silicon[12-14] have been explored by scientific researchers for use in LIBs. Among these materials, 2D transition metal chalcogenide compounds (MoS_2) have received great attention in view of their relatively weak van der Waals force, high active surface, large interlayer spacing, and abundant edges.[15-17] These extraordinary physicochemical properties can contribute to large pseudocapacitance and fast reaction kinetics. Nevertheless, the shortcomings of 2D nanomaterials are obvious, such as aggregation during the charge and discharge process. This will lead to the active sites being buried in the repeat lithiation/delithiation, thereby resulting in continuous capacity fading. Additionally, the ability of fast charge/discharge is hindered by the intrinsic poor conductivity.

It has been demonstrated that introducing pseudocapacitive charge storage in electrodes is a promising strategy to achieve the superior rate capability by overcoming the sluggish kinetics.[17-19] In particular, the pseudocapacitance refers to the redox reactions that occur on the surface or near-surface of the electrode materials, which can be intrinsic or external to the material. It is essential that constructing extrinsic pseudocapacitive materials with a tuned structure would be conducive to rapid ion transport and fast electron transfer and been experimentally demonstrated on some ultrathin nanosheets, ultrafine nanoparticles, nanowires, etc.[20-23] Although this method can facilitate the kinetics with the high pseudocapacitive behavior, the interior cycling life caused by the aggregation due to the Waals attraction is inevitable in the repeated insertion/extraction process. In this regard, an alternative method is decorating MoS_2 nanosheets with nanoparticles to moderate the surface energy and act as spacers to stabilize the MoS_2 nanosheets. Recently, much effort has been devoted to engineering MoS_2/nanocomposites with special designs to partly enhance the cycling stability.[24-27] However, the chemical bonding effect was not established, which is easily results in the collapse of composite structures due to the very limited interface efficiency between MoS_2 and nanocomposites. Therefore, the combination of 2D MoS_2 with pseudocapacitive nanoparticles are believed to be the promising composite materials with maximized interface contact for enhancing the performance of MoS_2-based LIBs.

In this work, we demonstrated a hierarchical 2D-2D nanoarchitecture composed of exfoliated MoS_2 nanosheets decorated with MoO_2 nanoparticles and 2D Ti_3C_2 MXene (MXene-MoS_2-MoO_2-C). In this unique structure, ultrafine MoO_2 nanoparticles can not only seperate the MoS_2 nanosheets to prevent the structural degradation but also guarantee the structural stability during the electrochemical performance. Additionally, the polymerization of polydopamine can not only be carbonized into N-doped carbon to enhance the conductivity of the composite materials, but can also provide the protective shell to strengthen the interface between MoS_2 and MoO_2 against partial surface collapse. Moreover, the addition of Ti_3C_2 MXene with a metallic conducting behavior can significantly improve the electronic conductivity of electrode and as a substrate to inhibit the agglomeration of the ultrathin MoS_2 nanaosheets during the growth process. Furthermore, the as-designed architecture can create plentiful edges and active sites, contributing to a high pseudocapacitives behavior and enabling the ultrafast kinetics. As expected, the as-prepared MXene-MoS_2-MoO_2-C electrode demonstrated outstanding cycling stability (over 800 cycling without capacity fading) and rate capability.

2. EXPERIMENTAL METHODS:

2.1. Preparation of MXene-MoS_2-MoO_2-C

$Ti_3C_2Ti_x$ MXene was obtained by HF etching of Ti_3AlC_2 powders. Subsequently, the $(NH4)_6Mo_7O_{24}{\cdot}4H_2O$ (0.8 g) and thiourea (1.42 g) were dissolved in deionized water and stirred vigorously to clear the solution. Then 0.12 g $Ti_3C_2Ti_x$ MXene was added to the above solution with constant stirring. Then the mixture was transferred into a Teflon-lined stainless-steel autoclave and heated to 200 ^oC for 24h. The MXene-MoS_2 powder was collected, washed several times with deionized water and ethanol, and dried at 80 ^oC in vacuum oven. After that, the as-prepared MXene-MoS_2 (0.5 g) was distributed in the mixed solutions (water/ethanol=8/15) and stirred for 10 mins. Then 0.3 mg $C_8H_{12}ClNO_2$ and 1.2 g $H_{24}Mo_7N_6O_{24}.4H_2O$ were added to the mixed solution. Subsequently, ammonia at a certain concentration was added to adjust the pH value to 10 at room temperature, and stirring was continued for 3-5 h. Finally, the precipitates were collected by centrifugation and calcined at high temperature (700 ^oC) for 2 h under argon atmosphere.

2.2. Material Characterization

The morphology and crystalline form of the as-prepared sample were characterized by scanning electron microscops, transmission electron microscopy, and X-Ray Diffraction (Bruker with a Cu Kα X-ray source). The elemental composition and calence state of the elements were detected by mains of X-ray photoelectron spectroscopy. The carbon state of the sample was determined by Raman spectra.

2.3. Electrochemical Measurements

The electrochemical performances were analyzed by assembling 2032-type coin cells. The as-prepared sample, conducting carbon, and CMC were mixed in water with a weight ratio of 8:1:1 to prepare the working electrode. Li metal and 1 M $LiPF_6$ in the mixture of EC/DMC (1:1) with 5 wt% FEC were used as the reference electrode and electrolyte, respectively. A constant-current cell tester (Land) was used to test the charge-discharge performance. The CV properties were determined using CHI605D electrochemical workstation.

3. RESULTS AND DISCUSSION

The typical fabrication process of MXene-MoS_2-MoO_2-C is demonstrated in the Scheme 1. The Ti_3C_2 MXene nanosheets were first obtained by etching Ti_3AlC_2 powder in concentrated hydrofluoric acid (HF). Then the layered MoS_2 nanosheets in the interlayer of the Ti_3C_2 sheets are realized through a simple hydrothermal process. Subsequently, ultrafine MoO2 nanocrystals were anchored on the MXene-MoS_2 nanosheets by the dopamine-directed growth with the assistance of self-polymerization reaction. The morphology and structure of the as-prepared composite materials were characterized by scanning electron microscopy (SEM) and transmission electron microscopy (TEM). Typical 2D Ti_3C_2 sheets with

a size of several microns are shown in Fig. 1. The layer spacing of Ti_3C_2 sheets becomes larger after etching by hundreds of nanometers, which provides a good space to accommodate the MoS_2 nanosheets. From Fig. 2 a, it can be found that the MoS_2 nanosheets are uniformly anchored on the both sides of Ti_3C_2 MXene.

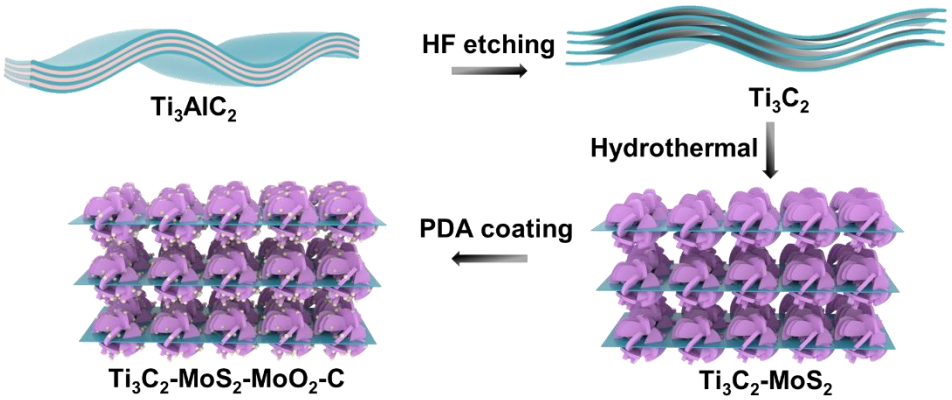

Scheme 1. Schematic illustration of the synthesis of the MXene-MoS_2-MoO_2-C

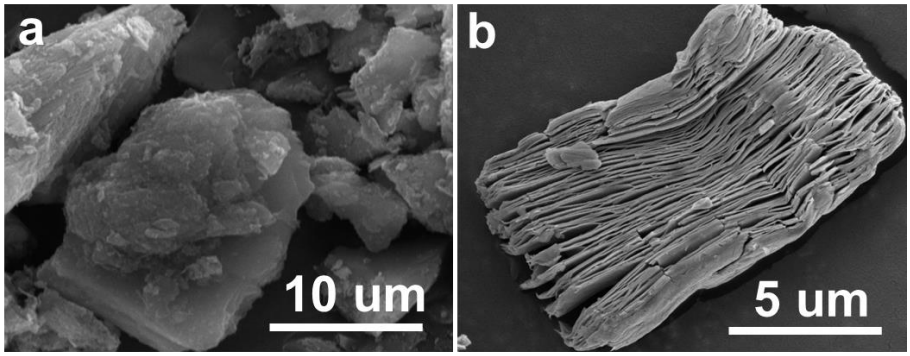

Figure 1 SEM images of MXene a) before etching and b) after etching

After coating with the MoO_2-carbon layer (Fig.2b), the hierarchical 2D structure of MoS_2 is still preserved well in the MXene-MoS2-MoO2-C composite, which is similar to that of MXene-MoS_2. The TEM image reveals that the MoS_2 nanosheets are fully covered with MoO_2 nanocrystals, which demonstrates the successful growth of the ultrafine MoO_2 nanopartices. The introduction of MoO_2 on the MoS_2 surface can effectively avoid the MoS_2 nanosheets stacks in the subsequent repeated charge/discharge process. To further confirm the structure of the MXene-MoS_2-MoO_2-C, high-resolution TEM (HRTEM) was performed. As shown in Fig. 2d, the interlayer spacing of 0.92 nm is detected, which is larger than that of typical MoS_2 nanosheets (0.63 nm). The enlarged interlayer space is mainly ascribed to the intercalation of polydopamine in the process of introducing MoO_2. The element distribution in as-prepared MXene-MoS_2-MoO_2-C sample is detected by EDX elemental mapping (Fig. 2e). It can be clearly seen that the C, Mo, O, S, and Ti elements are well dispersed in the sample, indicating the successful manufacture of MXene-MoS_2-MoO_2-C.

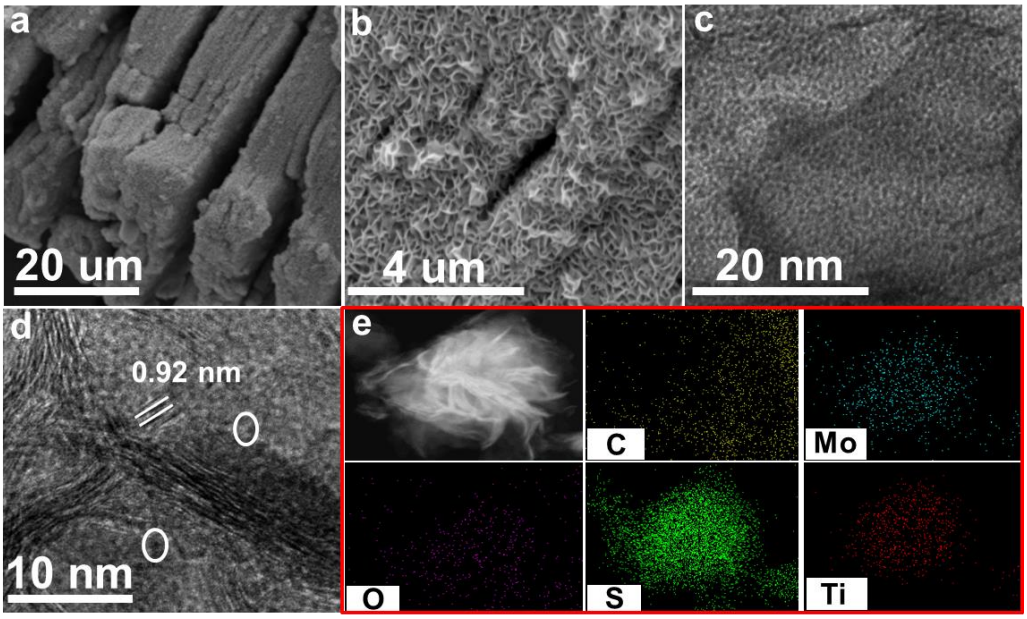

Figure 2. a) SEM image of MXene-MoS_2, b) SEM image, c-d) TEM images, and e) elemental mapping of the as-prepared MXene-MoS_2-MoO_2-C

The crystal structure and surface chemical state of MXene-MoS_2-MoO_2-C were investigated by X-ray powder diffraction (XRD) and X-ray photoelectron spectra (XPS). From the XRD patterns Fig. 4a), the characteristic peaks could be well indexed to 2H-MoS_2 (JCPDS No. 37-1492) and MoO_2 (JCPDS No. 73-1807). No obvious Ti_3C_2 MXene peaks are detected, the possible explanation may be that the diffraction peaks of Ti_3C_2 were overlaid by other peaks. The peaks located at 12.8°, 34.1°, 39.8°, 55.4°, and 58.9° can be ascribed to the (002), (102), (103), (106), and (110) planes of MoS_2, respectively. Notably, the peaks of (002) shifts to a small angele, indicating the enlarged interlayer distance due to the introduction of MoO_2 nanocrystals.[28] This result is in good agreement with the above HRTEM analysis. The XPS spectrum of MXene-MoS_2-MoO_2-C composite is shown in Fig. 3a, it exhibits the existence of C, O, Mo, S, N, and Ti elements. Fig. 4b shows the high resolution of Mo 3d spectrum, the corresponding peaks at binding energies of 229.5 and 232.9 eV can be attributed to the Mo $3d_{5/2}$ and Mo $3d_{3/2}$ of Mo^{4+} in MoS_2, respectively.[29] Additionally, there are two peaks located at binding energies of 230 and 233.1 eV, which can be explained by the Mo^{4+} of MoO_2. The small peak at 236.9 eV cossespond to the Mo^{6+}, which resulted from the formation of Mo-O-C bonds between the N-doped carbon and MoO_2.[30] The formation of this bond can strengthen the stability of the MXene-MoS_2-MoO_2-C composite to achieve the high electrochemical performance. The high resolution of S 2p (Figure 4c) can be fitted into two peaks at binding energies of 162.2 and 163.3 eV corresponding to the S $2p_{1/2}$ and S $2p_{3/2}$, respectively. The high resolution of O 1s (Fig. 4d) consists of three peaks, specially, the strong peak located at binding energy of 531.8 eV can be assigned to the Mo-O band, while the relatively weak peaks at binding energy of 530.6 and 533.8 eV attributed to the C-O and H-O bonds, respectively.

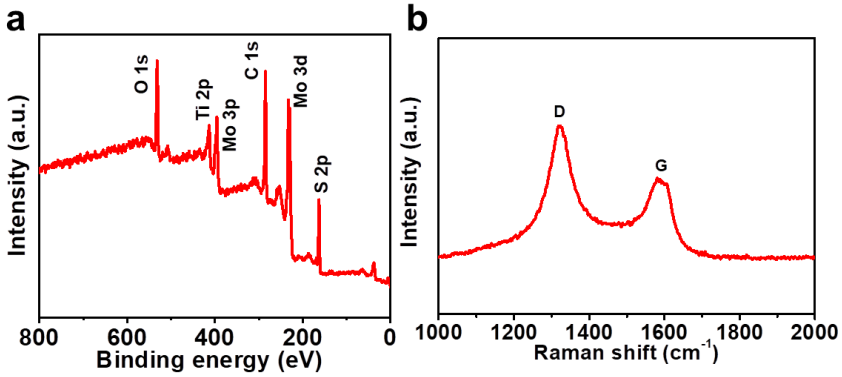

Figure 3. a) XPS spectrum, and b) Raman spectrum of MXene-MoS_2-MoO_2-C

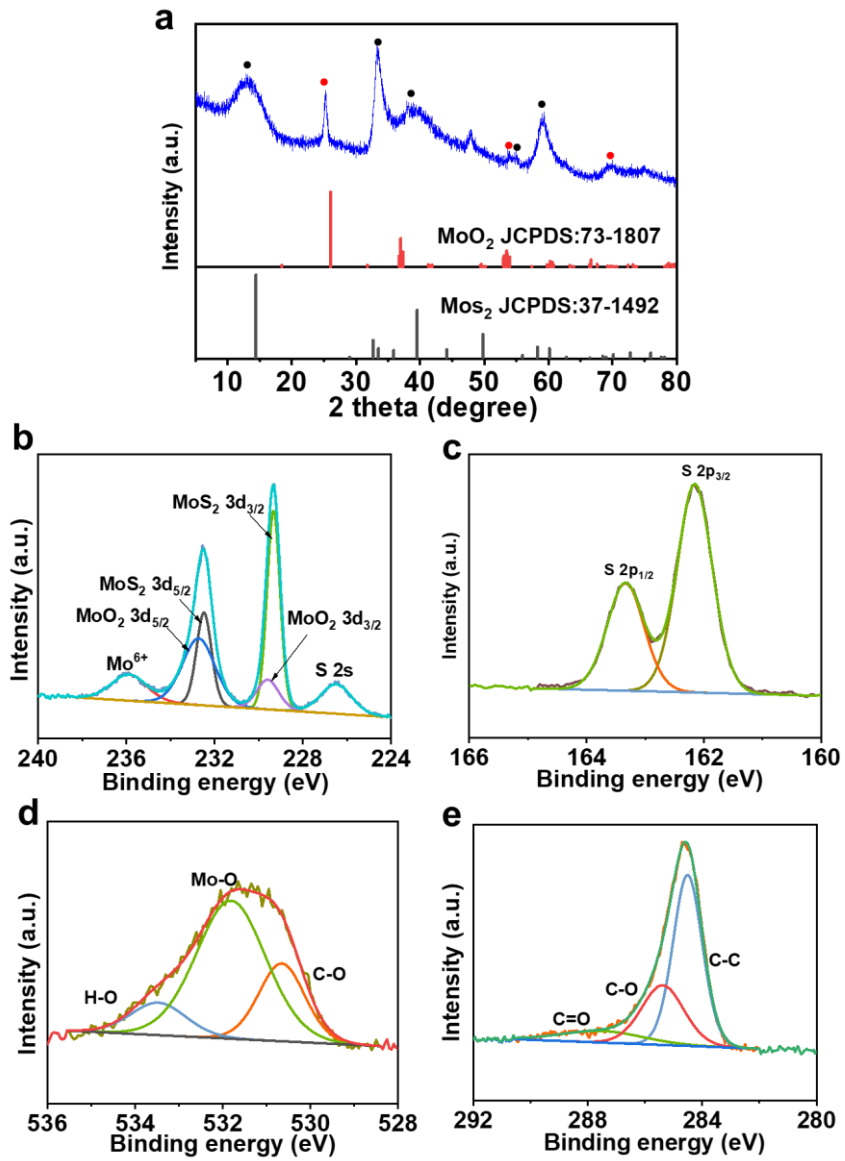

Figure 4. XRD patterns, and b-e) high-resolution XPS spectra of Mo 3d, S 2p, O 1s, and C 1s in the MXene-MoS_2-MoO_2-C

Three peaks at approximately of 284.4, 285.7, and 287.9 eV can be observed in the resolution of C1s (Fig. 4e), which can be attributed to the C-C, C-O, and C=O bonds, respectively. Raman spectroscopy was performed to examine the carbon state of the MXene-MoS_2-MoO_2-C. As shown in Fig. 3b, three obvious peaks are located at 1378 and 1598 cm^{-1}, which are the characteristic diffraction of D band (disordered carbon) and G band (graphitic carbon), respectively. The intensity of I_D/I_G reflects the degree of crystallinity of carbon materials.[31] The I_D/I_G of MXene-MoS_2-MoO_2-C is 1.28, which demonstrates the structural disorder and defects in carbon.

The lithium storage performance of the as-prepared MXene-MoS_2-MoO_2-C electrode was evaluated by assembly into 2032 coin-type half cells. The charge/discharge profiles of the MXene-MoS_2-MoO_2-C electrode at current of 1 A g^{-1} are shown in the Fig. 5. During the first cycle process, the electrode delivered the discharge specific capacity of 1310 mAh g^{-1} and charge specific capacity of 918 mAh g^{-1}, corresponding to an initial Coloumbic efficiency (ICE) of 70%. The irreversible capacity during the first cycle process is mainly caused by the formation of an irreversible solid electrolyte interphase (SEI) film on the surface of MXene-MoS_2-MoO_2-C electrode.[32] Furthermore, the CE increased quickly to 89% from the second cycle and remained stable at ~99% in the following cycles. When the electrode cycled for 50 cycles, the charge/discharge profiles were almost unchanged, demonstrating the good stability of MXene-MoS_2-MoO_2-C electrode.

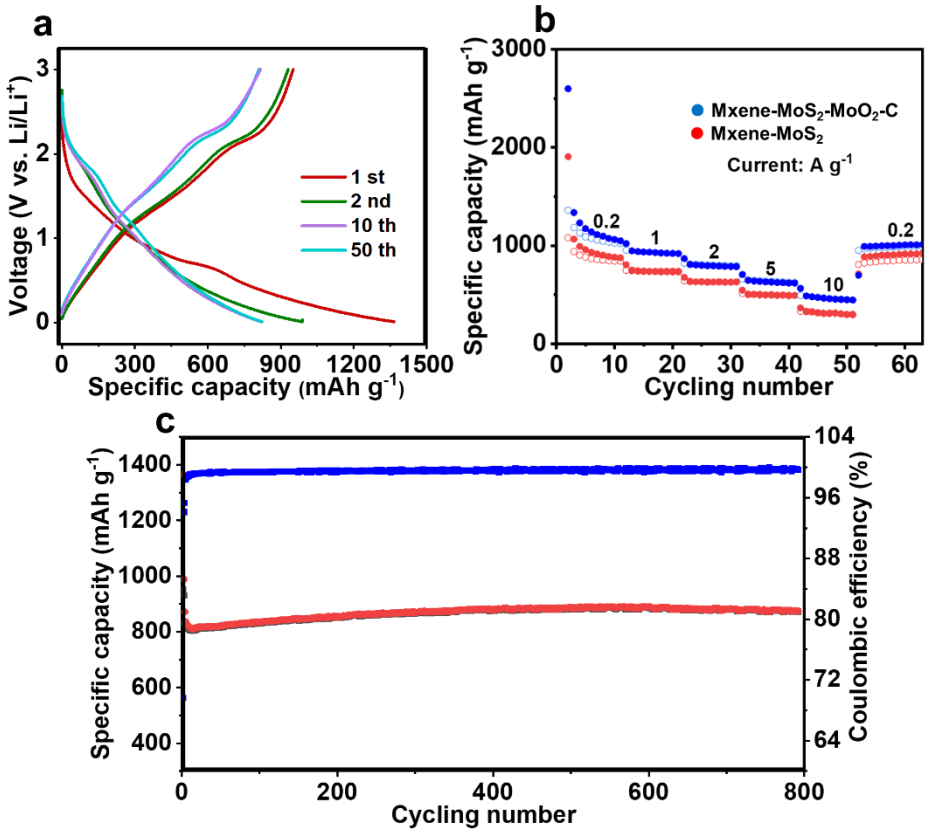

Figure 5. a) Charge/discharge profiles of MXene-MoS_2-MoO_2-C electrode, b) Rate capability of MXene-MoS_2-MoO_2-C and Mxene-MoS_2 electrodes, and c) the long-term cycling performance of MXene-MoS_2-MoO_2-C electrode at current of 1 A g^{-1}.

The rate capability of MXene-MoS_2-MoO_2-C electrode was explored at varying current densities from 0.2 to 10 A g^{-1}. From the Fig. 5b, the MXene-MoS_2-MoO_2-C electrode delivered specific capacity of 1080, 902, and 813 mAh g^{-1} at current density of 0.2, 1, and 2 A g^{-1}, respectively. Even at high current density of 5 and 10 A g^{-1}, high specific capacities of 743 and 685 mAh g^{-1} still can be reached for MXene-MoS_2-MoO_2-C electrode. When the current comeback to the initial 0.2 A g^{-1}, the specific capacity of MXene-MoS_2-MoO_2-C electrode can return to the ~1000 mAh g^{-1}. Such results illustrate that the MXene-MoS_2-MoO_2-C electrode possess good rate capability and can tolerate fast charge/discharge process. Meantime, the rate capability of MXene-MoS_2 electrode was also evaluated as comparison. The MXene-MoS_2 electrode only exhibited 823 and 716 mAh g^{-1} at current of 0.2 and 1 A g^{-1}, respectively, which are lower than those of MXene-MoS_2-MoO_2-C electrode. In addition to the rate capability, the long-term cycling stability is a key point to the application of LIBs. The cycling performance of MXene-MoS_2-MoO_2-C electrode is evaluated at current of 1 A g^{-1}, as shown in Fig. 5c. The capacity remains good well during the whole cycling without obvious capacity fading. After 800 cycles, the MXene-MoS_2-MoO_2-C electrode still maintains a high capacity of ~800 mAh g^{-1}, showing the excellent cycling stability. Based on the above discussion, the MXene-MoS_2-MoO_2-C electrode exhibits a comprehensive excellent electrochemical performance, which can be due to the structural strength and fast ion transfer rate. The comparision of the as-prepared electrode with reported literatures in Table 1.

The lithium storage mechanism was investigated by cyclic voltage (CV) at a scan rate of 0.1 mV s^{-1}. The initial five CV curves of the MXene-MoS_2-MoO_2-C electrode at a potential of 0.01~3 V are shown in Fig. 6a. In the first cathodic process, there are two reduction peaks located at 1.48 V and 0.65 V, which can be attributed to the insertion of lithium ions into MoS_2 to form Li_xMoS_2 and the conversion of Li_xMoS_2 into metallic Mo and formation of SEI, respectively.[33, 34] For the initial anodic process, the oxidation peak at 1.28 V can be observed, which is due to the oxidation of Mo to MoS_2. The other peak at 2.18 V related to the extraction of Li^+ from Li_2S. During the subsequent reduction scan, the two new peaks located at 1.8 and 1.18 V appear, which can be ascribed to the reduction of S and Mo, respectively.[35-36] The shift of the cathodic peaks can be explained by the formation of SEI film during the initial cathodic scan. From the second scan process, the subsequent CV curves nearly overlap, illustrating the excellent reaction reversibility of as-prepared MXene-MoS_2-MoO_2-C electrode. The electrochemical kinetics of MXene-MoS_2-MoO_2-C electrode were further explored by the CV curves at different scan rates from 0.1 to 2 mV s^{-1}. As shown in Fig. 6b, all curves maintain a similar shape with increasing of scan rate. The lithium ion storage mechanism can be separated into interaction process and surface pesudocapactive process. The relationship between measured current (i) and scan rates (v) can be described by the following equation[37]:

$$i = av^b$$

where *a* and *b* are the adjustable values. In particular, the value of b can be calculated from the slope of log *i vs.* log *v* plots. When the value of b is 1, it represents the charge storage is totally controlled by the capacitive behavior. The b value of 0.5 indicates that the diffusion behavior dominates the charge storage process. It can be seen from Fig. 6c shows that the b value is higher than 0.8 during the whole anodic process, indicating that the Li^+ insertion is mainly affected by the capacitive process for the fast kinetics. In addition, the capacitive contribution to the whole process can be quantitatively analysed by the following equation[38]:

$i=k_1v+k_2v^{1/2}$

where the k_1v and $k_2v^{1/2}$ represent diffusion-controlled process and pseudocapacitive behaviour, respectively. As illustrated in Fig. 6d, the capacitive behavior (red colour) plays a larger role in the whole charge storage process with a ratio of 84% at the scan rate of 0.2 mV s^{-1}. Such high pseudocapacitive contribution of MXene-MoS_2-MoO_2-C electrode can be ascribed to the hierarchical heterostrucutre, which can not only effectively prevent the aggregation of MoS_2 nanosheets during the charge/discharge process but also provide more active sites for Li^+ adsorption. The high contribution of pseudocapacitive is conducive to fast reaction kinetics, which is probably a significant reason for the impressive rate capability.

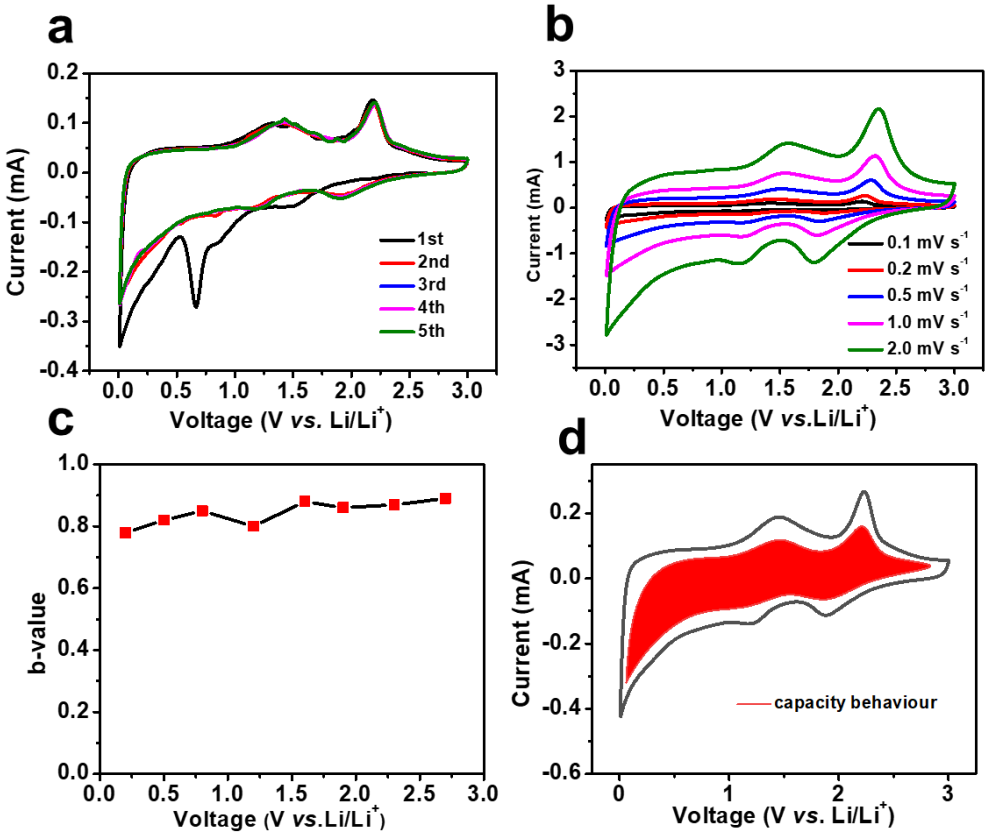

Figure 6. Figure 4. a) CV curves at 0.1 mV s^{-1} of MXene-MoS_2-MoO_2-C electrode, b) CV curves at different scan rates from 0.1 to 2 mV s^{-1} of MXene-MoS_2-MoO_2-C electrode, c) the b-value at different corresponding voltage MXene-MoS_2-MoO_2-C electrode, and the capacitive contribution at scan rate of 0.2 mV s^{-1} MXene-MoS_2-MoO_2-C electrode.

Table 1. Comparision of the as-perpared electrode in this paper with reported literatures.

Samples	Rate	Cycling performance
MXene-MoS_2-MoO_2-C	685 mAh g^{-1} at 10 A g^{-1}	100% capacity retention

		after 800 cycles at 1 A g^{-1}
CNT@MoS_2 NSs [39]	473 mAh g^{-1} at 10 A g^{-1}	82% capacity retention after 60 cycles at 0.1 A g^{-1}
MoS_2 NSs/CNP[40]	678 mAh g^{-1} at 10 A g^{-1}	100% capacity retention after 100 cycles at 0.1 A g^{-1}
C@MoS_2 MS[32]	486 mAh g^{-1} at 1 A g^{-1}	80% capacity retention after 50 cycles at 0.1 A g^{-1}
MoS_2@TiO_2 hybrid[41]	523 mAh g^{-1} at 1 A g^{-1}	60% capacity retention after 50 cycles at 0.1 A g^{-1}
TiO_2 MoS_2 nanohybrid[42]	433 mAh g^{-1} at 1 A g^{-1}	70% capacity retention after 100 cycles at 0.1 A g^{-1}

4. CONCLUSION

In conclusion, we designed and constructed ultrafine MoO_2 nanoparticles decorated MoS_2 naonosheets, incorporating N-doped carbon grown on Ti_3C_2 MXene sheets, by a hydrothermal and self-polymerization method. First, the N-doped carbon not only can enhance the conductivity of the electrode, but can also play an important role in maintain the structural integrity; in addition, the ultrafine MoO_2 nanoparticles can effectively avoid the aggregation of 2D MoS_2 nanosheets during the repeated charge/discharge process and reduce the ion diffusion length to facilitate the ion transport; moreover, the synergetic effect and enhance pseudocapacitive of the 3D hierarchical structure can enable the rapid ions/electrons transfer and improve the reaction kinetics. Benefitting from the unique 3D structure, the as-prepared MXene-MoS_2-MoO_2-C electrode exhibited excellent rate capabilities and good cycling stability when used as the anode in LIBs. This work may provide a successful route for designing advanced electrode materials for high-rate and long-life LIBs.

ACKNOWLEDGEMENTS
The authors appreciate Ms. Xue Ding (Instrumental analysis center, Shanghai Jiaotong University) for XPS test.

References

1. J. Jian, L. Yuanyuan, L. Jinping, H. Xintang, Y. Changzhou, X.W.D. Lou, *Advanced Materials*, 24 (2012) 5166-5180.
2. J. Xiao, Q. Li, Y. Bi, M. Cai, B. Dunn, T. Glossmann, J. Liu, T. Osaka, R. Sugiura, B. Wu, J. Yang, J.-G. Zhang, M.S. Whittingham, *Nature Energy*, 5 (2020) 561-568.
3. P.K. Nayak, L. Yang, W. Brehm, P. Adelhelm, *Angewandte Chemie-International Edition*, 57 (2018) 102-120.
4. Z. Jian, B. Zhao, P. Liu, F. Li, M. Zheng, M. Chen, Y. Shi, H. Zhou, *Chemical Communications*, 50 (2014) 1215-1217.
5. T. Jiang, F. Bu, X. Feng, I. Shakir, G. Hao, Y. Xu, *ACS Nano*, 11 (2017) 5140-5147.
6. H. Gao, T. Zhou, Y. Zheng, Q. Zhang, Y. Liu, J. Chen, H. Liu, Z. Guo, *Advanced Functional Materials*, 27 (2017) 43.
7. B. Wang, Y. Cheng, H. Su, M. Cheng, Y. Li, H. Geng, Z. Dai, *Chemsuschem*, 13 (2020) 4078-4085.
8. D.-C. Zuo, S.-C. Song, C.-S. An, L.-B. Tang, Z.-J. He, J.-C. Zheng, *Nano Energy*, 62 (2019) 401-409.
9. Y. Xu, Y. Zhu, Y. Liu, C. Wang, *Advanced Energy Materials*, 3 (2013) 128-133.
10. Y. Ren, Z. Liu, F. Pourpoint, A.R. Armstrong, C.P. Grey, P.G. Bruce, *Angewandte Chemie-International Edition*, 51 (2012) 2164-2167.
11. H. Ren, R. Yu, J. Wang, Q. Jin, M. Yang, D. Mao, D. Kisailus, H. Zhao, D. Wang, *Nano Letters*, 14 (2014) 6679-6684.
12. M. Zhang, L. Li, X. Jian, S. Zhang, Y. Shang, T. Xu, S. Dai, J. Xu, D. Kong, Y. Wang, X. Wang, *Journal of Alloys and Compounds*, 878 (2021) 160396.
13. H. Wang, J. Fu, C. Wang, J. Wang, A. Yang, C. Li, Q. Sun, Y. Cui, H. Li, *Energy & Environmental Science*, 13 (2020) 848-858.
14. S. Smidstrup, T. Markussen, P. Vancraeyveld, J. Wellendorff, J. Schneider, T. Gunst, B. Verstichel, D. Stradi, P.A. Khomyakov, U.G. Vej-Hansen, M.-E. Lee, S.T. Chill, F. Rasmussen, G. Penazzi, F. Corsetti, A. Ojanpera, K. Jensen, M.L.N. Palsgaard, U. Martinez, A. Blom, M. Brandbyge, K. Stokbro, *Journal of Physics-Condensed Matter*, 32 (2020) 3244.
15. W.-J. Zhang, K.-J. Huang, *Inorganic Chemistry Frontiers*, 4 (2017) 1602-1620.
16. J. Wu, F. Ciucci, J.-K. Kim, *Chemistry-A European Journal*, 26 (2020) 6296-6319.
17. T. Wang, S. Chen, H. Pang, H. Xue, Y. Yu, *Advanced Science*, 4 (2017),18754.
18. X.-Y. Yu, H. Hu, Y. Wang, H. Chen, X.W. Lou, Angewandte Chemie-International Edition 54 (2015) 7395-7398.
19. S. Ding, J.S. Chen, X.W. Lou, *Chemistry-A European Journal* 17 (2011) 13142-13145.
20. S. Lou, X. Cheng, Y. Zhao, A. Lushington, J. Gao, Q. Li, P. Zuo, B. Wang, Y. Gao, Y. Ma, C. Du, G. Yin, X. Sun, *Nano Energy*, 34 (2017) 15-25.
21. S. Liu, H. Jia, L. Han, J. Wang, P. Gao, D. Xu, J. Yang, S. Che, *Advanced Materials* 24 (2012) 3201-3204.
22. H. Liu, Z. Bi, X.-G. Sun, R.R. Unocic, M.P. Paranthaman, S. Dai, G.M. Brown, *Advanced Materials*, 23 (2011) 3450-.
23. X. Han, Q. Meng, X. Wan, B. Sun, Y. Zhang, B. Shen, J. Gao, Y. Ma, P. Zuo, S. Lou, G. Yin, *Nano Energy* 81 (2021)2345.
24. J. Ru, T. He, B. Chen, Y. Feng, L. Zu, Z. Wang, Q. Zhang, T. Hao, R. Meng, R. Che, C. Zhang, J. Yang, *Angewandte Chemie-International Edition* 59 (2020) 14621-14627.
25. S. Kim, M. Hankel, W. Cha, G. Singh, J.M. Lee, I.Y. Kim, A. Vinu, *Nano Energy* 72, (2020) 1237.
26. H. Geng, J. Yang, Z. Dai, Y. Zhang, Y. Zheng, H. Yu, H. Wang, Z. Luo, Y. Guo, Y. Zhang, H. Fan, X. Wu, J. Zheng, Y. Yang, Q. Yan, H. Gu, *Small*, 13 (2017)1421.
27. H. Chen, J. He, G. Ke, L. Sun, J. Chen, Y. Li, X. Ren, L. Deng, P. Zhang, *Nanoscale* 11 (2019) 22134-22134.

28. C. Wang, J. Jiang, Y. Ruan, X. Ao, K. Ostrikov, W. Zhang, J. Lu, Y.Y. Li, *ACS Applied Materials & Interfaces* 9 (2017) 28441-28450.
29. L. Yang, S. Wang, J. Mao, J. Deng, Q. Gao, Y. Tang, O.G. Schmidt, *Advanced Materials* 25 (2013) 1180-1184.
30. J. Wang, H. Zhou, M. Zhu, A. Yuan, X. Shen, *Journal of Alloys and Compounds* 744 (2018) 220-227.
31. S.S. Bukalov, R.R. Aysin, L.A. Leites, V.E. Eremyashev, *Carbon*, 64 (2013) 548-550.
32. L. Zhang, X.W. Lou, *Chemistry-A European Journal* 20 (2014) 5219-5223.
33. C.-Y. Wei, P.-C. Lee, C.-W. Tsao, L.-H. Lee, D.-Y. Wang, C.-Y. Wen, *ACS Applied Energy Materials* 3 (2020) 7066-7072.
34. J. Pei, H. Geng, E.H. Ang, L. Zhang, X. Cao, J. Zheng, H. Gu, *Nanoscale* 10 (2018) 17327-17334.
35. J. Bai, B. Zhao, J. Zhou, J. Si, Z. Fang, K. Li, H. Ma, J. Dai, X. Zhu, Y. Sun, *Small*, 15 (2019).16823
36. C. Ma, Z. Xu, J. Jiang, Z. F. Ma, T. Olsen, H. Xiong. *Journal of Materials Chemistry* A, 8 (2020) 11011-11018.
37. J. Wang, J. Polleux, J. Lim, B. Dunn, *Journal of Physical Chemistry* C 111 (2007) 14925-14931.
38. J.-Y. Liao, V. Chabot, M. Gu, C. Wang, X. Xiao, Z. Chen, *Nano Energy*, 9 (2014) 383-391.
39. S.J. Ding, J.S. Chen, X.W. Lou, *Chem-Eur J*, 17 (2011) 13142-13145.
40. H.S. Li, X.Y. Wang, B. Ding, G. Pang, P. Nie, L.F. Shen, X.G. Zhang, *Chemelectrochem*, 1 (2014) 1118-1125.
41. X. Xu, Z.Y. Fan, S.J. Ding, D.M. Yu, Y.P. Du, *Nanoscale*, 6 (2014) 5245-5250.
42. X.Q. Zhu, C. Yang, F. Xiao, J.D. Wang, X.T. Su, *New J Chem*, 39 (2015) 683-688